

AFRL-AFOSR-UK-TR-2014-0005



Design, Fabrication, and Characterization of Metamaterials for Transformation Optics and Focusing Applications

Professor Uriel Levy

**Hebrew University of Jerusalem
Mount Scopus
Jerusalem, Israel 91905**

EOARD Grant 10-3096

Report Date: February 2014

Final Report from 01 September 2010 to 31 August 2013

Distribution Statement A: Approved for public release distribution is unlimited.

**Air Force Research Laboratory
Air Force Office of Scientific Research
European Office of Aerospace Research and Development
Unit 4515, APO AE 09421-4515**

REPORT DOCUMENTATION PAGE				Form Approved OMB No. 0704-0188	
<small>Public reporting burden for this collection of information is estimated to average 1 hour per response, including the time for reviewing instructions, searching existing data sources, gathering and maintaining the data needed, and completing and reviewing the collection of information. Send comments regarding this burden estimate or any other aspect of this collection of information, including suggestions for reducing the burden, to Department of Defense, Washington Headquarters Services, Directorate for Information Operations and Reports (0704-0188), 1215 Jefferson Davis Highway, Suite 1204, Arlington, VA 22202-4302. Respondents should be aware that notwithstanding any other provision of law, no person shall be subject to any penalty for failing to comply with a collection of information if it does not display a currently valid OMB control number.</small> PLEASE DO NOT RETURN YOUR FORM TO THE ABOVE ADDRESS.					
1. REPORT DATE (DD-MM-YYYY) 11 February 2014		2. REPORT TYPE Final Report		3. DATES COVERED (From – To) 1 September 2010 – 31 August 2013	
4. TITLE AND SUBTITLE Design, Fabrication, and Characterization of Metamaterials for Transformation Optics and Focusing Applications				5a. CONTRACT NUMBER FA8655-10-1-3096	
				5b. GRANT NUMBER Grant 10-3096	
				5c. PROGRAM ELEMENT NUMBER 61102F	
				5d. PROJECT NUMBER 	
6. AUTHOR(S) Professor Uriel Levy				5d. TASK NUMBER 	
				5e. WORK UNIT NUMBER 	
7. PERFORMING ORGANIZATION NAME(S) AND ADDRESS(ES) Hebrew University of Jerusalem Mount Scopus Jerusalem, Israel 91905				8. PERFORMING ORGANIZATION REPORT NUMBER N/A	
9. SPONSORING/MONITORING AGENCY NAME(S) AND ADDRESS(ES) EOARD Unit 4515 APO AE 09421-4515				10. SPONSOR/MONITOR'S ACRONYM(S) AFRL/AFOSR/IOE (EOARD)	
				11. SPONSOR/MONITOR'S REPORT NUMBER(S) AFRL-AFOSR-UK-TR-2014-0004	
12. DISTRIBUTION/AVAILABILITY STATEMENT Distribution A: Approved for public release; distribution is unlimited.					
13. SUPPLEMENTARY NOTES 					
14. ABSTRACT <p>The research covered four primary areas: manufacture of on-chip transformation optics (metamaterials), metamaterials as superabsorbers, thermal characterization of metamaterials and nanophotonic devices, and use of metamaterials for plasmonic focusing and splitting. MANUFACTURE: The team designed, fabricated, and experimentally demonstrated an on-chip device for 2d plasmonic transformation optics on a chip. This was done by generating subwavelength dielectric features on a flat metallic surface; by adjusting the spacing of gratings, the team modified the index of refraction in the region of the "lens", successfully focusing surface plasmon polaritons (SPP). SUPERABSORBERS: The team used the Rigorous Coupled Wave Analysis (RCWA) method to study the interaction of incident plane waves with periodic metamaterials with alternating double-positive and double-negative materials, showing very strong effects on light propagation even if the structure's thickness is much smaller than the incident wavelength. This demonstrated the feasibility of absorbing light by very thin films of metamaterials with zero average refractive index. THERMAL CHARACTERIZATION: Since metamaterials can concentrate electromagnetic energy, nanoscale-level self-heating issues can be significant problems with nanoscale device development. The team used Scattering Thermal Microscopy to demonstrate a direct measurement of the temperature distribution of a silicon photonic chip using a thermocouple probe. By constructing a device (a doped Micro Ring Resonator (MRR)) and shining light tuned to MRR resonances, self-heating was induced, noting that when the laser is tuned to the MRR resonance there is a substantial rise in the thermal signal within the ring, but out of resonance the rise in thermal signal is marginal. Repeating the experiment with an undoped device, which showed no significant self-heating. PLASMONIC FOCUSING: The team constructed a device capable of splitting and focusing surface plasmon polaritons into different locations depending on the polarization of the excitation source, showing its possible use as a plasmonic quadrant detector or possible beam splitter, showing that the device split orthogonally polarized light into orthogonal directions.</p>					
15. SUBJECT TERMS EOARD, Metamaterials, Transformation Optics, surface plasmon polaritons, plasmonics					
16. SECURITY CLASSIFICATION OF:			17. LIMITATION OF ABSTRACT SAR	18. NUMBER OF PAGES 19	19a. NAME OF RESPONSIBLE PERSON Victor Putz
a. REPORT UNCLAS	b. ABSTRACT UNCLAS	c. THIS PAGE UNCLAS			19b. TELEPHONE NUMBER (Include area code) +44 (0)1895 616013

Final Report for EOARD grant 10-3096

Principal Investigator: Uriel Levy

Department of Applied Physics

School of Engineering

Hebrew University of Jerusalem, Jerusalem, Israel, 91904

Phone: +972-2-6584256. Fax: +972-2-6584256.

(In collaboration with David Smith, Duke University, USA)

December 2013

1 - Metamaterials for transformation optics

We have designed, fabricated and experimentally demonstrated an on chip configuration for the realization of transformation optics on a chip. The concept of operation is to generate subwavelength dielectric features on top of a flat metallic surface. Specifically, we were focused on the realization of graded index focusing device. This device, schematically depicted in Fig. 1(a), is realized by electron-beam lithographically defined subwavelength features in PMMA, allowing to control the local effective index of refraction of the SPP mode propagating along the grooves. Because of the space-variant nature of the structure, Bloch theorem cannot be applied in its direct form. Instead, the local effective refractive index for the Magnetic out of plane polarization (TM) is calculated using the Effective Medium Theory (EMT).

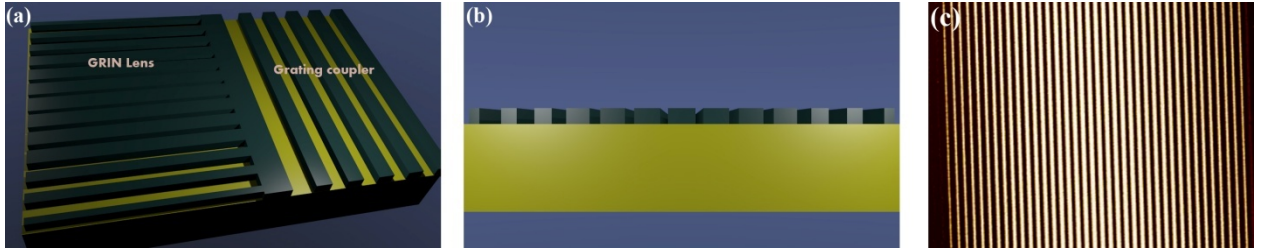


Fig 1: (a) overview of the device including: grating coupler, free space propagation section and the GRIN lens; (b) Schematic cross section of the lens. The period is kept constant whereas the duty cycle is varying in space; (c) AFM measurement showing the profile of the grooves

In order to design our SPP based planar graded index lens, we first calculate the effective index of the SPP mode supported by a slab of Au\PMMA (200nm thick)\Air. Next, we use the EMT to calculate the duty cycle modulation of the grating according to Eq. 1 to obtain a parabolic profile of the refractive index for TM polarization.

$$n_{TM}^{(2)} = \sqrt{(n_{TM}^{(0)})^2 + \frac{1}{3} \left(\frac{\Lambda}{\lambda} \pi f (1-f) \left(\frac{1}{n_1^2} - \frac{1}{n_2^2} \right) n_{TE}^{(0)} (n_{TM}^{(0)})^3 \right)}$$

$$n_{TM}^{(0)} = \frac{n_1 n_2}{\sqrt{f n_2^2 + (1-f) n_1^2}} \quad n_{TE}^{(0)} = \sqrt{f n_1^2 + (1-f) n_2^2} \quad (1)$$

where: $\lambda = 1.55 \mu m$ $\Lambda = 400 nm$ $n_1 = 1$ (Air) $n_2 = 1.18 + 0.0029i$ (the effective index of the slab mode). Light is coupled to the SPP mode using a grating coupler.

Schematic drawing of the structure is shown in Fig. 1(a), whereas a schematic cross section showing the varying duty cycle of the graded index structure is presented in Fig. 1(b). We couple the light to SPP using a grating coupler as can be seen in Fig. 1(a).

After fabrication, we performed an AFM measurement to confirm the topography of the lens (Fig. 1(c)). In order to measure the lens we use Near-field Scanning Optical Microscopy (NSOM) as can be seen in Fig. 2. As can be observe, the phase front curvature of the propagating SPP mode is converging towards the focal spot, after which it flips direction and becoming diverging, as expected (Fig. 2a). In addition, it can be seen that the beam size is decreasing towards the focus, as denoted by the solid lines in Fig. 2b. The capability of focusing SPPs along the metal-dielectric interface by using this relatively simple device is expected to promote the field of 2-D plasmonic based transformation optics, with variety of potential applications including for example focusing, steering, and routing of SPPs as well as plasmonic based cloaking.

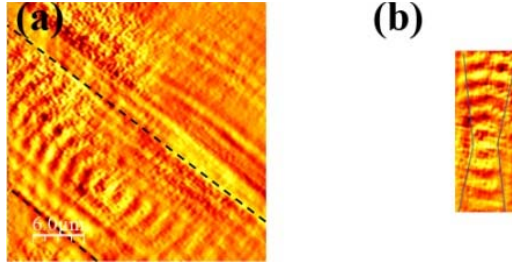


Fig 2: (a) Overview of the device. The lens is bounded between the dashed black lines. It can be seen that the phase front curvature of the SPP mode flips from convergence to divergence in the vicinity of the focus. (b) Enlargement Zoom in on the central section of panel a. The flipping from converging to diverging phase front can be clearly observed. The solid line denotes the effective beam size, showing a minimum around the focus.

Publications:

- 1 - Meir Grajower, Gilad Lerman, Ilya Goykhman, Boris Desiatov, Avner Yanai, David R. Smith and Uriel Levy, "Subwavelength Plasmonics for graded-index optics on a chip," Optics Letters 38, 3492-3495 (2013).
- 2 - Meir Grajower, Gilad Lerman, Ilya Goykhman, Boris Desiatov, Avner Yanai, David R. Smith and Uriel Levy, "Plasmonic graded-index planar lens based on subwavelength features in the effective index regime," CLEO (2012)

2 - Metamaterials for enhancing light matter interactions – super absorbers

Here, we use the Rigorous Coupled Wave Analysis (RCWA) method to study the interaction of an incident plane wave with periodic metamaterials consisting of alternating double positive (DPS) and double negative (DNG) materials. The incident angle is normal to the direction of periodicity. For such a configuration we show that very strong effects on light propagation can be obtained even if the structure's thickness is much smaller than the incident wavelength. As a result, a giant and narrow band of absorption is obtained, with a sharp resonance peak even for a very thin layer, ~two orders of magnitude thinner than the vacuum wavelength. We thus coin this structure as a "super-absorber".

To get better understanding of the physics of this interaction we analyzed the modes in the structure shown schematically in Fig. 3(a). The structure consists of alternating layers of DPS and DNG layers with unit cell

L and thickness h . The average refractive index is close to zero: $\bar{n} = \frac{1}{L} \int_0^L n(x) dx \approx 0$. We found that this

structure has very narrow transmission peaks at the discrete frequencies where Fabry-Perot interference occurs. However, this result was obtained for an infinitely thick structure ($h=\infty$) with illumination in the direction of periodicity (x direction). The interesting question is what would happen if we illuminate a thin structure with finite thickness by normally incident plane wave propagating in the z direction? To answer this question, we have used RCWA to calculate the transmission, reflection and absorption of the structure.

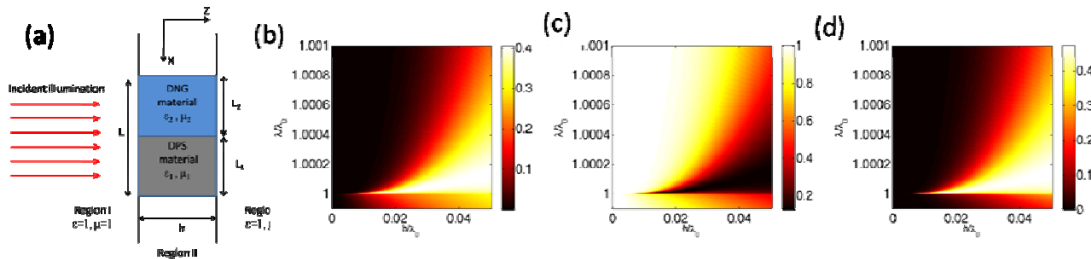


Fig. 3(a) Schematic of a unit cell, and RCWA calculation of: (b) transmission (c) reflection (d) absorption as function of h/λ_0 and λ/λ_0

Schematic of a unit cell, and RCWA calculation of: (b)

The results are shown in Fig. 3(b-d), calculated for the case where the material parameters in the periodic layer are $\epsilon_1=1-0.001i$, $\epsilon_2=-1-0.001i$, $\mu_1=1$, $\mu_2=-1$ and $L=\lambda_0$ where λ_0 is the resonant wavelength as will be shown. It is seen that for the normalized layer thickness of $\sim h/\lambda_0=0.01$ and $\lambda=\lambda_0$, a very narrow absorption peak is obtained, resulting in absorption of $\sim 50\%$ of the incident energy. To gain further understanding of the physics behind the obtained transmission/absorption/reflection maps we plot (Fig. 4) the field

distribution within the metamaterial structure and its vicinity, for $h=0.01L$. First, it can be seen from Figs. 2(a,b) that at resonance ($\lambda=L$) in regions I and III the diffracted wave occupies precisely a single unit cell and therefore can be identified as the Fabry-Perot mode, which is consistent with the choice of $L \approx \lambda$. It is seen that in the slightly off-resonance case ($\lambda=1.001L$) shown in Fig. 2(c), the mode no longer occupies a unit cell and therefore the mode is no longer a Fabry Perot one. The very narrow lineshape (Q factor of the order of $\sim 1 \times 10^6$ for $h/\lambda_0=0.01$) is explained by the sensitivity of the Fabry Perot resonance, where small change in wavelength shifts the domination to the Bragg regime over the Fabry Perot regime. The high Q-factor can be also understood by observing the magnetic field distribution of the Fabry Perot mode (Fig. 4(a)) having an odd symmetry with respect to the x-axis. In contrast, the reflected and transmitted plane waves have even magnetic field distribution, resulting in a vanishing overlap integral between them and the Fabry-Perot mode, and thus giving rise to “dark modes” which typically have very large Q-factors for structures with small inherent losses.

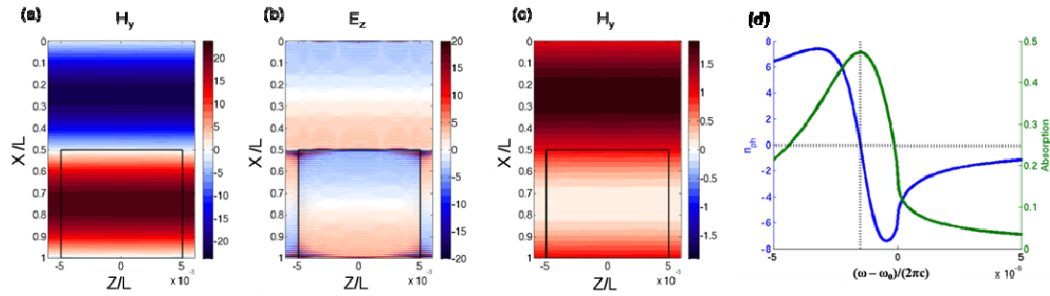


Fig. 4. Real part of the field profiles in the NIM grating, calculated using the RCWA method (a) H_y field component at resonance ($\lambda=L$), (b) E_z field component at resonance ($\lambda=L$) (saturated color scale) (c) H_y field for the off-resonance case ($\lambda=1.001L$). The black rectangles denote the region of the DNG layer. (d) Phase index (blue line, left y-axis) and absorption (green line, right y-axis) as function of $\omega - \omega_0$ normalized by $2\pi c$, calculated for $h=0.01L$. The correspondence between the absorption peak and the zero phase index is marked by the crossing of the dashed lines.

To gain further insight, it is also instructive to evaluate the phase index (n_{ph}) of light propagation in the z -direction, in the resonant frequencies. The phase index is calculated according to: $n_{ph} = \frac{c}{h} \frac{\Delta\phi}{\omega}$, where $\Delta\phi$ is

the phase difference between the transmitted and incident waves, and $\omega=2\pi c/\lambda$. In Fig. 4(d), we have plotted both the absorption and the phase index as function of frequency near resonance for $h=0.01L$. It can be seen that at the peak of absorption, n_{ph} crosses zero (marked in Fig. 4(d) by the crossing of the dotted lines), indicating an asymptotically infinite phase velocity at this wavelength. This indicates that at the absorption peak, the fields are evenly distributed between the DPS and DNG media. Since the phase velocity in both media is opposite, inside the grating there is full cancelation of phase accumulation in the z direction. In summary, we demonstrate the feasibility of absorbing light by very thin films of metamaterials with zero average refractive index. This property may show useful for applications related to light matter interactions, solar cells, and efficient remote transfer of energy by optical methods.

Publications:

- 1 - Avner Yanai, Meir Orenstein and Uriel Levy, “Giant resonance and absorption in ultrathin metamaterials,” CLEO (2012)
- 2 - A. Yanai, M. Orenstein, and U. Levy, “Giant resonance absorption in ultra-thin metamaterial periodic structures,” Opt. Express 20, 3693-3702 (2012).

3 – Thermal characterization of metamaterials and nanophotonic devices

Nanoscale thermal characterization of photonic devices is important for understanding the underlying physics of self heating at the nanoscale, as well as for the development of advance on chip photonic components and circuits. Indeed, being able to directly measure the temperature of integrated photonic devices at the nanoscale may pave the way for developing approaches for controlling heat dissipation, designing thermally stable devices and enable their dense integration on chip.

To cope with this need, we use Scanning thermal microscopy (SThM) and demonstrate a benchmark of direct measurement of the temperature distribution of silicon photonic chip using a thermocouple probe. Specifically, we focus on the thermal properties of a doped micro ring resonator, of the same type which has been demonstrated for active photonics applications such as photonic modulators. The temperature mapping of the system is recorded when the ring is at resonance and out of resonance. The results indicate a significant self heating which must be taken into account.

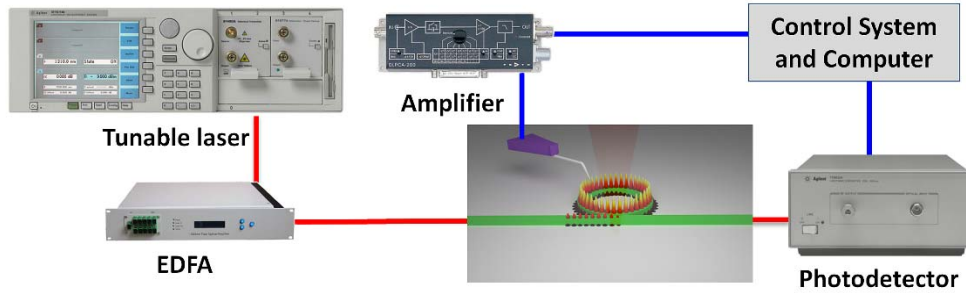


Fig.4. Schematic representation of the experimental setup for the simultaneous thermal and optical transmission measurement

To demonstrate a nanophotonic device self-heating we have constructed the experimental setup depicted in Fig. 4. A TE polarized light derived from a tunable laser (Agilent 81680A) operating around 1550nm wavelength was coupled into the tapered ends of the chip waveguides using polarization maintaining lensed fibers. The device was not optimized for minimal insertion loss (estimated loss is about 15dB per facet). The laser signal was amplified using erbium doped fiber amplifier (EDFA, RED-C) and the output light was detected by an InGaAs photodetector (HP 81634B). As mentioned before, our device of choice was a Micro Ring Resonator (MRR) with a single bus waveguide coupled to the ring. The ring radius is 6 μ m and the gap in the coupling region is 200nm. The device was fabricated on a silicon-on-insulator substrate with 2 μ m oxide layer below separating between the waveguide structure and the silicon substrate. The waveguides width was set to 450nm and their height was 250nm including a 20nm silicon rib as shown schematically in Fig.5(c). In Fig. 5(a) a Scanning Electron Micrograph (SEM) of the fabricated microring is shown. The temperature measurement was done using thermocouple probes purchased from Nanonics and mounted on a Nanonics MultiView-4000 head. The probes consist of a Pt wire running through a metal-coated glass nano-pipette and slightly protruding over its edge. The external Au coating extends over the Pt wire, forming the thermocouple junction between the two metals. Typical tip diameter at the apex is 150-300nm. The thermocouple probe was connected to the control system through a low-noise trans impedance amplifier (FEMTO DLPCA-200).

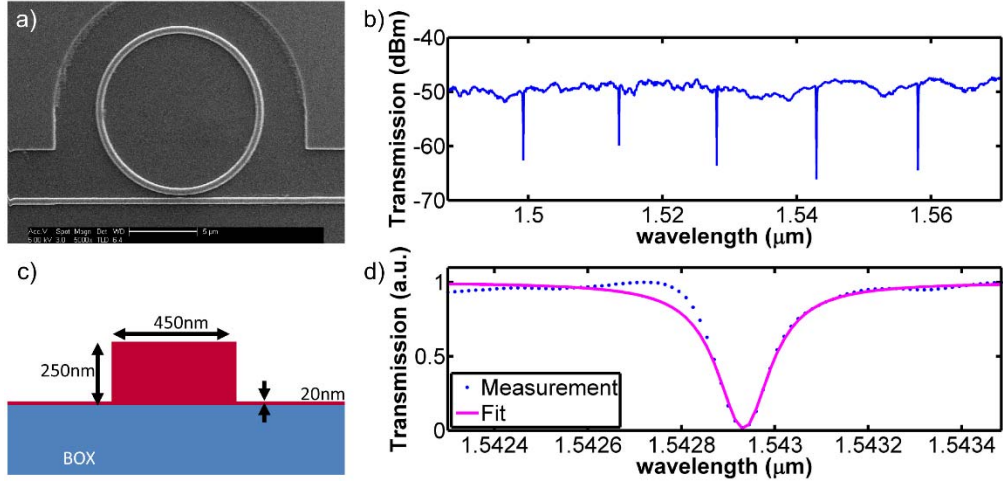


Fig.5. (a) Top view SEM image of the measured silicon micro ring resonator (b) Measured transmission spectrum of the device (c) Schematic cross section diagram of the silicon waveguide (d) Lorentzian fit to a single resonance dip used for obtaining the resonator's quality factor

First, the transmission spectrum of the device was measured by scanning the tunable laser and collecting the data in the detector. The results in Figs. 5(b) and 5(d) show nice resonance dips with quality factor and finesse of $Q \approx 11000$ and $F \approx 110$, respectively.

Next, we turn into measuring the effect of self heating. The structure is Boron-doped with concentration level of $N = 5 \cdot 10^{17}$ atoms/cm³, which is comparable to typical doping concentrations of active silicon photonic devices [22-26]. For such doping concentration, the self heating of the device is originated primarily from free carrier absorption (FCA). When 1550nm wavelength light is propagating in the waveguide, a portion of it is absorbed and dissipated as heat. The absorption coefficient was calculated using Soref empirical formula [27] $\alpha_{FC} = (8.5 \cdot N_e + 6.0 \cdot N_h) \cdot 10^{-18}$ to be 3cm⁻¹. The effect of self heating is enhanced when the wavelength of light is tuned to one of the resonant wavelengths of the MRR due to the intensity buildup inside the resonator. The intensity buildup inside the resonator was calculated to be $I_{Ring} = 50 \cdot I_{in}$ [28] and the power loss to heat is $P_{Heat} = 0.01 \cdot P_{Light}$, where P_{Light} is the optical power inside the resonator.

To observe the effect of self heating, the laser wavelength was tuned to one of the MRR resonances. A thermocouple tip (200 nm in diameter) was placed in close proximity to the structure and a raster scan was executed. As a control experiment we repeated this measurement when the wavelength was detuned to 3nm away from the MRR resonance and also when the laser was turned off. The results are shown in Figs. 6(a)-6(f). It is apparent from Fig. 6(a) that when the laser is tuned to the MRR resonance there is a substantial rise in the thermal signal within the ring. Interestingly, maximum signal is obtained around the edges of the MRR waveguide. This is shown very clearly by taking a cross section across the waveguide of the MRR in Fig. 6(d). The reason for this interesting finding is related to the perturbation of the tip, as explained in more details in one of the subsequent sections. When the wavelength is tuned to be out of resonance, see Fig. 6(b), the rise in thermal signal is only marginal (shown by the corresponding cross section in Fig. 6(d)). The slight increase may be explained by the small on-resonance contribution of the amplified spontaneous emission (ASE) coming from the EDFA. This can be eliminated by the use of a band pass filter. In addition, we extracted from Figs. 3(a)-(b) cross sections of the thermal signal along the bus waveguide as shown in Fig. 6 (e). The result indicates that the temperature along the waveguide is approximately flat in case that the system is out of resonance. In case that the system is in resonance, the thermal signal undergoes a sudden drop at the coupling region and then stabilizes at a lower level. This is because the light is coupled into the ring and experiences a significant loss, such that only a small portion of the input signal is coupled back into the waveguide. A dark measurement (without the presence of an optical signal) serves as a control measurement, indicating that the electronic cross-talk in the system (cross talk between the error channel of the AFM and the signal channel) is small, as presented in Fig. 6(c).

Finally, we repeated the experiment with a similar un-doped device as shown in Fig. 6(f). For that purpose we selected a silicon MRR with identical geometrical dimensions and with very similar parameters

($Q \approx 14000$, $F \approx 140$). In this device we expect the losses to arise mostly as a result of scattering from bends and defects in the structure, with very little absorption. Thus heat generation is expected to be small. Thermal scans were executed with identical scan parameters and with similar optical intensity propagating in the waveguide, when the system was kept in-resonance and out-of-resonance. As expected, no traces of temperature rise were observed near the ring or over the bus waveguide in neither of the cases within the precision limits of our system.

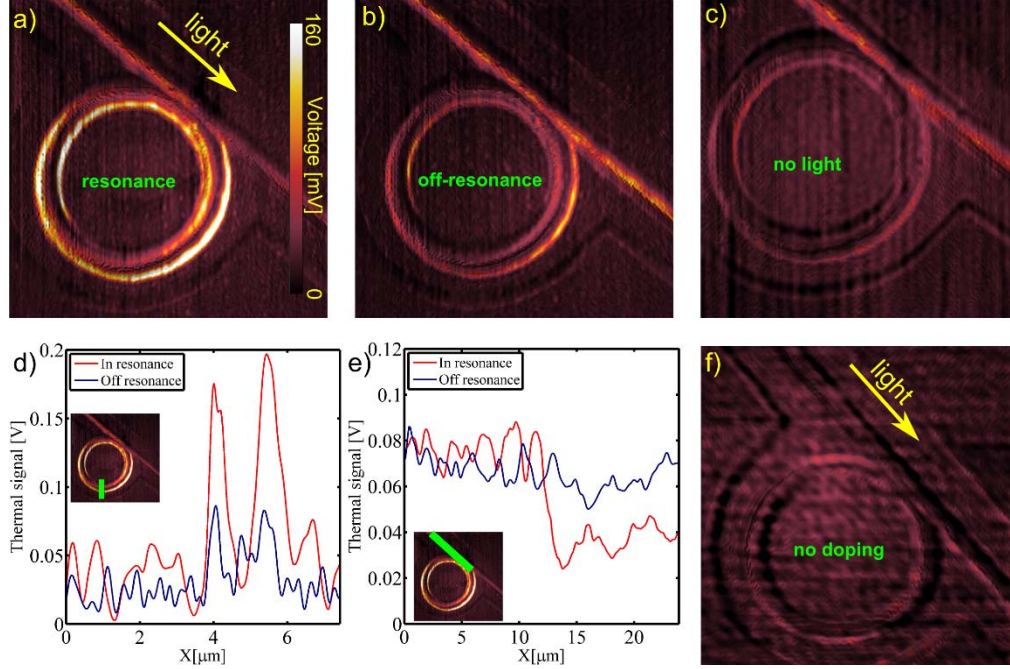


Fig. 6. Thermal images of the doped silicon MRR (a) in-resonance (b) out-of-resonance and (c) with no optical signal (laser turned off). (d) Cross section of the thermal signal over the ring waveguide (e) Cross section of the thermal signal along the bus waveguide. The cross section direction is shown in the inset. (f) A thermal image of the un-doped silicon MRR in resonance. The green wide lines in Fig. 6d and Fig. 6e show the location of the cross section in the image.

Journal publications and conference presentations:

- 1 – M. Tzur, B. Desiatov, I. Goykhman, M. Grajower, and U. Levy, "High resolution direct measurement of temperature distribution in silicon nanophotonics devices," *Opt. Express* 21, 29195-29204 (2013).
- 2 - B. Desiatov, I. Goykhman, M. Tzur and U. Levy, "Nanoscale Temperature Mapping of Plasmonic Devices," *Nano Meta*, Seefeld (2013), Paper SUN4o.2.
- 3 - B. Desiatov, I. Goykhman, M. Tzur, and U. Levy, "Nanoscale Temperature Mapping of Plasmonic Devices," SPP6, Ottawa (2013). Paper Tu-28-P-21

4 – Plasmonic focusing and splitting

With the significant progress in research and technology of plasmonic and metamaterials based devices, it becomes clear that integration of several devices and functionalities is essential for the implementation of these technologies in real life applications. Following this motivation, we hereby demonstrate a device which is capable of splitting and focusing surface plasmon polaritons (SPPs) into different locations depending on the polarization of the excitation source. Having such a device in hands, one can control the propagation direction and focal position of the SPPs simply by modulating the polarization of the illuminating source. Therefore, our plasmonic device may play a role in plasmonic circuiting where there is a need to control the flow of SPPs and focus them into specific locations e.g. in order to couple them into a plasmonic waveguides or focus them into several spots for multi-channel microscopy applications.

Following the capability of polarization dependent splitting and focusing of SPP's, we propose and demonstrate the possible use of this plasmonic structure as a plasmonic quadrant detector. Owing to its small foot print, such a miniaturized four quadrant detector is expected to show features such as low dark current and fast operation speed, both are important in real time accurate tracking of optical beams.

Fig. 7 shows a scanning electrons microscope (SEM) micrograph of the fabricated device. As can be seen, it is composed of four identical nanometric slits milled into a silver layer having a quarter circle shapes and arrange in a way to form a “pin cushion” structure. The radius of each slit is 10 microns and its width is 250 nm. When light is impinging on the slits SPPs are generated on the surface. These SPPs can interfere constructively at the center of each of the quarter circle slits. Clearly, the coupling strength of light into SPPs depends on the polarization of light with respect to the direction of the slit. Only TM polarized light (i.e. magnetic field parallel to the slit and electric field perpendicular to the slit) will contribute to the excitation of SPPs.

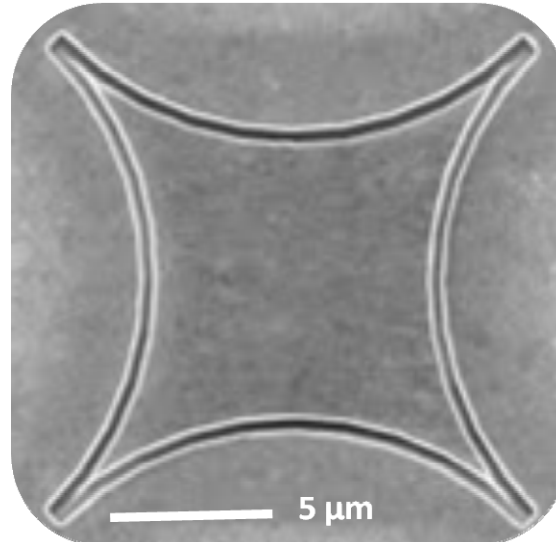


Fig. 7 An SEM micrograph of a “pin cushion” structure with circles radius of 10 microns and slit width of 250 nm.

Assuming a constant electric field impinging on the slit, SPPs will be generated according to the projection of the polarization direction along the normal to the slit so each point along the slits is a point source for the diffraction pattern with polarization based amplitude. We calculated the electric field distribution generated by the “pin cushion” structure for the vacuum wavelength of $\lambda_0=1064$ nm. At this wavelength the wave vector of a plasmonic mode running on the interface between silver and air is nearly equal to the vacuum wavenumber, with negligible loss over the propagation distances that are considered here.

Figures 8 (a) and (b) show the calculated intensity of the z-polarized (out of plane) electric field component $|E_z|^2$ for the case of illuminating a “pin cushion” structure with circles radius of 10 microns by a linearly polarized field at the wavelength of 1064 nm. Due to the fact that SPPs are generated only from sections where the incident polarization is TM with regard to the slits it can be seen that two focal spots are formed along a line parallel to the incident polarization direction (shown by the white arrow). If the polarization direction is rotated by 90 degrees the two focal spots will appear at the centers of the other two circles and the whole field pattern will be rotated by 90 degrees, as can be seen in fig 8 (b). This effect makes the “pin cushion” structure a very attractive plasmonic device as it can be used as a plasmonic polarized beam splitter, splitting the SPPs into perpendicular directions, depending on the polarization content of the incident light, and in addition it focuses the SPPs into small spots, e.g. for the purpose of launching plasmonic signals into small plasmonic waveguides, enhancing light matter interactions, or for detection by a small plasmonic detector. Fig. 8(c) and (d) show the near-field scanning optical microscope (NSOM) measurements on the surface of a “pin cushion” device corresponding to the simulation results shown in Fig. 8(a) and (b) respectively. The two focal spots along the polarization direction and the nice agreement to the simulation results are easily noticed. The high intensity apparent in the measurements near the slits of the “pin cushion” structures is probably due to the localization of energy in the slits and the

direct radiation of the light from the slit into free space. This effect was not taken into account in the simulations.

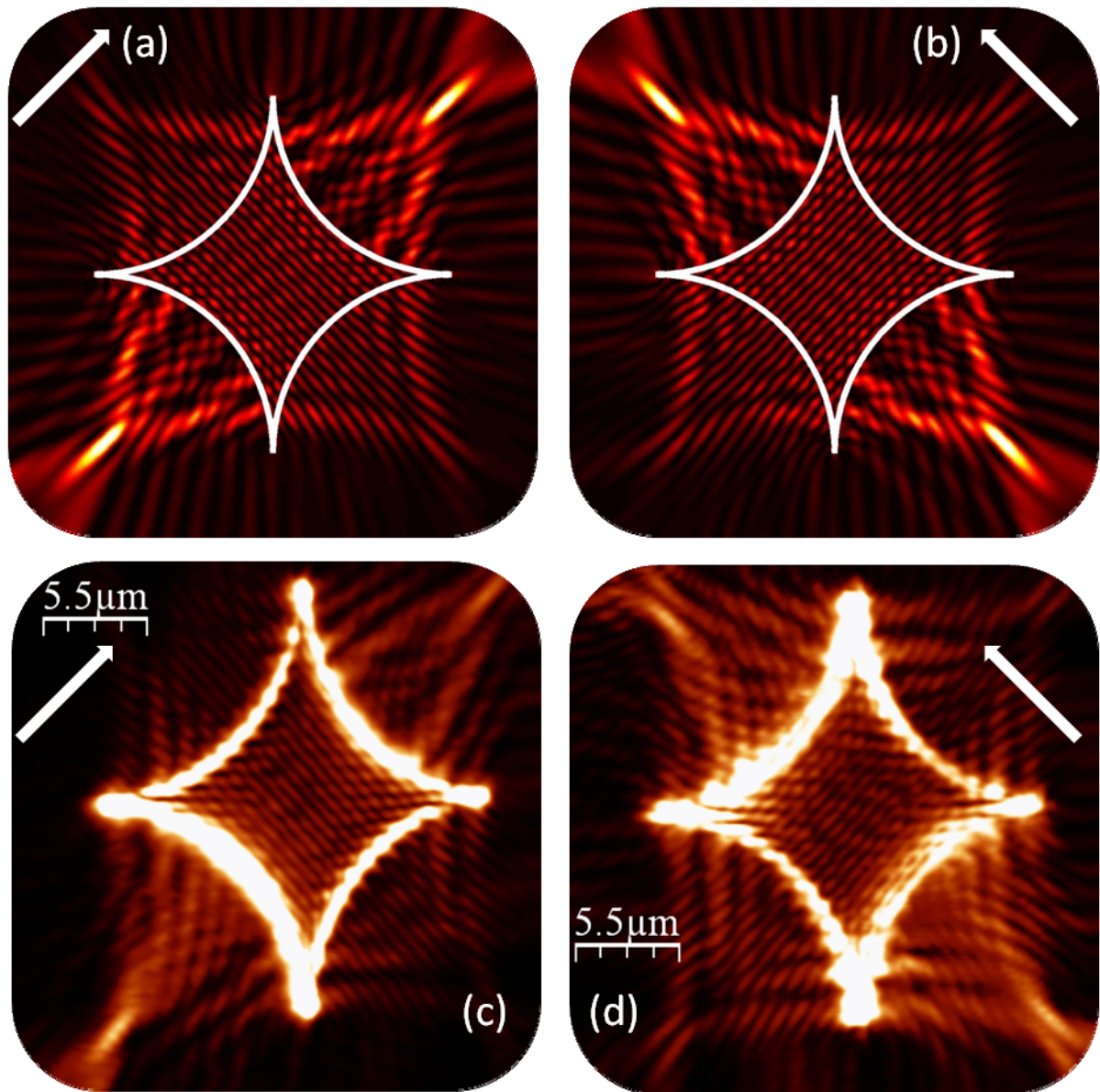


Fig. 8. A “pin cushion” structure with circles radius of 10 microns and slit width of 250 nm illuminated with linearly polarized 1064 nm light. (a) and (b) – computer simulation results showing the out of plane field distribution intensity, (c) and (d) experimental NSOM measurements, respectively. The white arrows represent the polarization direction of the illuminating light.

As discussed and demonstrated, the locations of the focal spots generated by the “pin cushion” device are determined by the geometry of the slits and the direction of polarization of the incident beam of light. One can use this feature for additional applications other than splitting and focusing of SPPs. Specifically, the “pin cushion” device may become an attractive choice as a plasmonic four quadrant detector. When illuminated with either circularly polarized or unpolarized light, four focal hot spots are obtained, each located at the center of the corresponding quarter circle of the “pin cushion” structure. Yet, the intensity of each focal spot may vary, depending on the position of the incident beam with respect to the structure. If the incident Gaussian beam is located at the center of the “pin cushion” structure, the intensity of the four

focal spots is expected to be identical. Nevertheless, if the Gaussian beam is shifted from the center of the structure the intensity at each focal spot will increase or decrease depending on the new position of the incident beam. Measuring the intensity at each of the four focal spots by on-chip detectors located at the center of the four quarter circles provides useful information on the position of the beam and may enable to use the “pin cushion” structure as a plasmonic quadrant detector capable of measuring the relative position of the illuminating beam with respect to the center of the structure.

While the integration of nanodetectors into the structure is beyond the scope of this work, the feasibility of the proposed concept is demonstrated by illuminating the “pin cushion” structure with a circularly polarized Gaussian beam, scanning its position with regard to the structure, and performing NSOM scans for several representing cases of relative shift between the center of the illuminating beam and the center of the device. From these scans, we were able to extract the intensity at each of the four focal spots for each of these representing cases. Figure 9 (a-d, i-l) show the obtained NSOM measurements for several positions of the illuminating beam with regards to the center of the device. Figure 9 (e-h) and (m-p) show the corresponding computer simulations. As can be seen the intensity pattern varies significantly when the center of the illuminating beam is shifted from the center. These variations are the basis for the operation of the “pin cushion” device as a four quadrant detector.

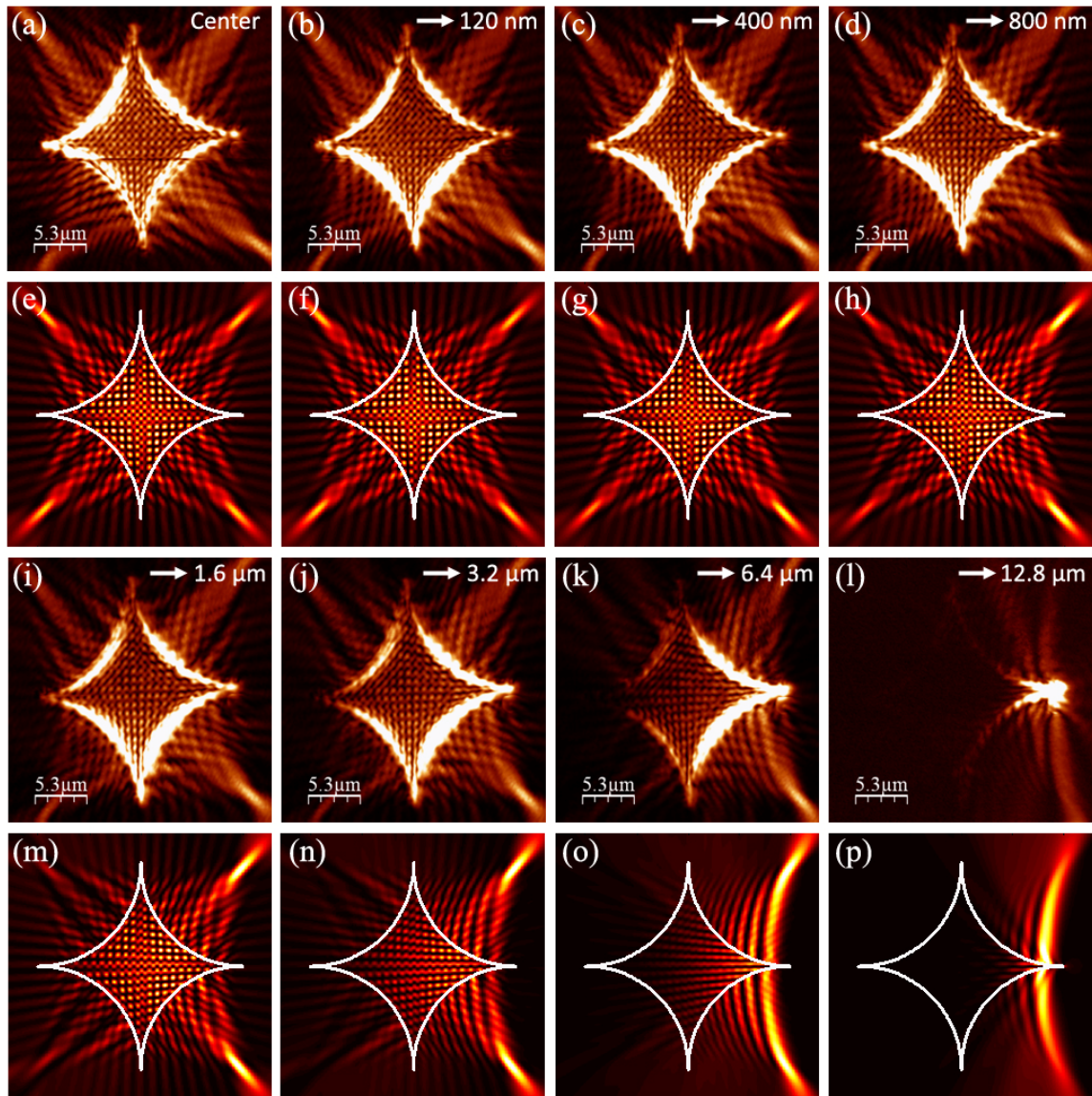


Fig. 9. (a-d) and (i-l): NSOM measurements for several values of relative shifts between the device and the illuminating beam. The shift values are noted in the figure. (e-h) and (m-p): the corresponding computer simulations showing the expected intensity pattern of the out of plane electric field component.

To summarize this section, we have proposed, fabricated and demonstrated a “pin cushion” shaped plasmonic device capable of splitting SPPs based on the polarization of the illuminating beam of light, direct them to different directions and focus them into a small focal spot. Using computer simulations and near field experimental characterization it was shown that this structure split orthogonally polarized light into orthogonal directions. Furthermore, by illuminating the device with circularly polarized light, four focal spots are obtained at the centers of each of the quarter circles composing the “pin cushion” device. The relative intensity of the four focal spots varies as a function of the relative shift between the illuminating beam of light and the center of the structure. This property is used to demonstrate the potential use of our device as a plasmonic quadrant detector.

Following the previous demonstration, it is clear that polarization plays a dominant role in the nanophotonics structures. Specifically, it was already shown that radially polarized light is the preferred choice for various applications, e.g. tight focusing of light. Unfortunately, having multiple sources of radially polarized light is a very challenging task. Hereby we provide a path towards overcoming this deficiency by experimentally demonstrating the coupling of an array of radially polarized beams to surface plasmons polaritons (SPP's), generating a periodic array of coherent, radially polarized “plasmonic focal spots”. This is achieved by passing a single radially polarized beam through a Dammann grating, effectively splitting the beam to multiple, equal-intensity radially polarized diffraction orders. These diffraction orders are then tightly focused on a uniform metal film, facilitating their coupling into SPPs. Using a near field scanning optical microscope (NSOM) we observed the propagation of SPP modes originated by the radially polarized diffraction orders and the coherent interactions between these “plasmonic sources” as they propagate on the metal film.

When light is tightly focused through glass onto a thin metal film which is evaporated on the glass, and phase-matching conditions are met, it can be coupled to SPP's propagating on the other interface of the metal, i.e. the interface between metal and air. Under such circumstances, it has been shown that when the incident light is radially polarized, the SPP near-field will take the form of Bessel functions with a “plasmonic focal-spot” on the optical axis, with high confinement of optical field and energy:

Here \hat{z} is the out-of-plane field component ($z=0$ is the metal-air interface), and \hat{r} is the in-plane component, β is the SPP propagation coefficient and k_D is the SPP decay coefficient in the \hat{z} direction. In the experimental setup we shall later describe, for illumination at wavelength $\lambda = 975$ nm, we have calculated $|\beta| = 6.49 \mu\text{m}^{-1}$; $|k_D| = 0.77 \mu\text{m}^{-1}$, meaning that E_z is the dominant field component, and it is ~ 10 times stronger than E_r .

However, when measuring these fields with an aperture type NSOM, the E_z component is weakly coupled to the tip and therefore the measurement typically consists of a combination of both field components, with ratio that is depending on the specific NSOM probe. In some cases, the dominant field component will be, surprisingly, the in-plane field component - E_r . In the following we will be consistent with previous papers, assuming that the transverse field component (which is proportional to the transverse derivative of the z polarized field component) is dominant.

When tightly focusing multiple beams diffracted from a diffraction grating, each beam propagates with a slightly different angle (measured from the optical axis and defined by the ratio of wavelength to the period of the grating), and should be focused to a different point in the focal plane (see Fig. 10). If each of these beams is radially polarized, we expect to obtain multiple sources of plasmonic hot spots propagating along the metal-air interface, each with a cylindrical symmetry with respect to the origin of the plasmonic spot. Furthermore, due to the coherence between these hot spots, they are expected to interfere, generating an interference pattern which depends on their distances, the plasmonic wavelength and the initial phase of each plasmonic hot spot. This effect is observed and discussed in the following sections.

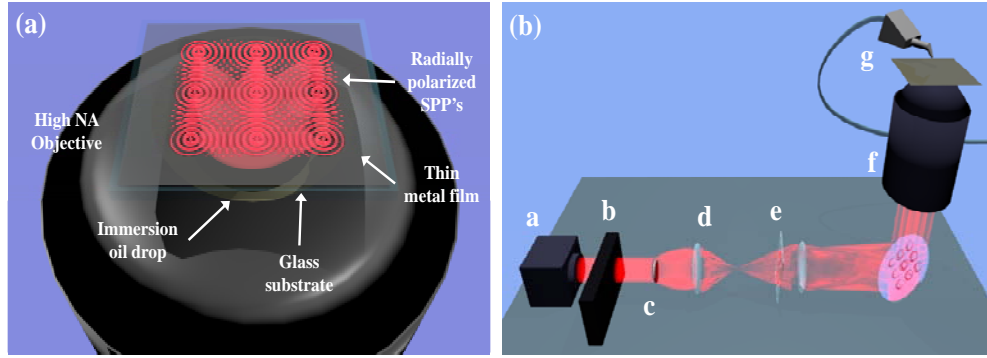


Fig. 10. (a) Illustration of SPP coupling scheme: Radially polarized laser beams are focused by a high NA oil-immersion microscope objective onto a microscope cover slip coated with a 50 nm thick Gold (Au) film. SPP's are coupled to the Gold-Air interface. (b) Experimental setup: A laser beam (a) propagates through a radial polarization converter (b). The center of the beam is blocked by metallic disk (c), the beam is expanded by an inverted telescope (d) and diffracted by a Damann phase grating (e). The diffraction orders propagate towards a 100X, NA=1.4 microscope objective (f), focused on to the thin metal film, and measured by an aperture NSOM (g).

To calculate the obtained plasmonic field propagating along the metal-air interface we assumed 9 plasmonic sources, set in a 3X3 array with a spacing of 8 μm . Each source generates a Bessel field pattern. To better fit the simulation to the actual experimental scenario (described in more details in the next two sections), we assumed that the amplitude of the central spot is larger by a factor of $\sqrt{2}$ from the amplitudes of the other spots. The phase of each plasmonic source is resulted from the properties of the grating generating the diffraction orders. The phase of each diffraction order was numerically calculated from the Fourier transform of the grating structure. For our structure, the phase difference between the (nth, mth) diffraction order and the 0th order is:

The obtained plasmonic field pattern, calculated for the vacuum wavelength of 975 nm, is given by the vector sum of the contributions from all 9 plasmonic sources. The intensity of the calculated field is presented in Fig. 11. For the calculation we assumed attenuation coefficient of $\frac{1}{20} \mu\text{m}^{-1}$. While this loss coefficient is higher than the predicted Ohmic loss for a single gold-air interface, we believe it better reflects a real life scenario, in which additional losses due to scattering and metal imperfections are evident.

As can be observed from the distinct interference patterns, the plasmonic sources are interacting coherently with each other. The strength of these interactions depends on the distance between the spots, with respect to the attenuation length. Additionally, we note that the pattern is not symmetric under rotation by 90 degrees. This is because of the phase difference between the various diffraction orders.

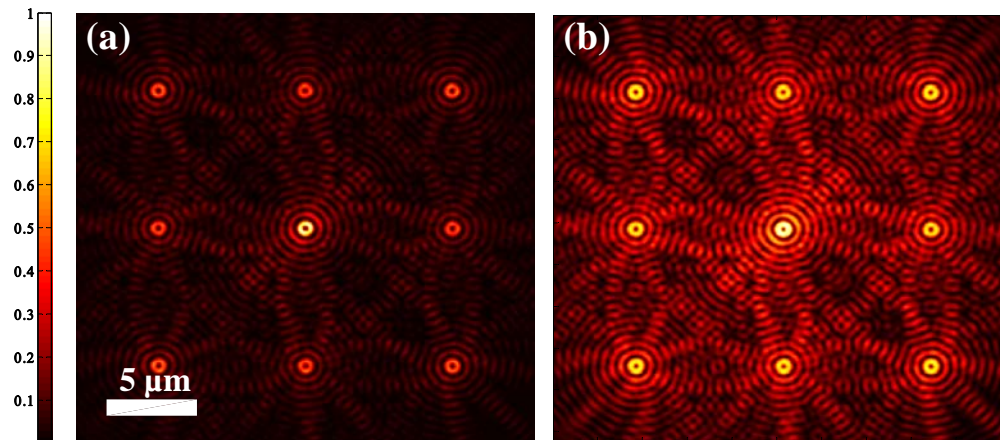


Fig. 11. Calculated intensity of the transverse plasmonic electric field showing the interaction of 9 radially polarized plasmonic sources propagating on a gold-air interface. a) Normal intensity color scale. b) Logarithmic color scale for better visibility of details.

To experimentally observe the effect of coherent interactions and to demonstrate the generation of multiple radially polarized plasmonic sources, we constructed the experimental setup depicted in Fig. 10

(b). A collimated, linearly polarized beam derived from a diode laser source at the wavelength of 975 nm (Optoenergy Inc.), propagates through a radially polarized converter (Arcoptix S.A.).

Behind the polarization converter the center of the beam is blocked by a glass plate with a metallic disk on it. The position of the mask along the light propagation axis is chosen to satisfy imaging condition between the mask and the back aperture of the microscope objective, and the disk size is chosen such that it will block most of the back aperture of the objective. Next, the beam is expanded by an inverted telescope which is designed such that its front focal plane coincides with the back aperture of a microscope objective. A Dammann phase grating is situated between the telescope's lenses splitting the beam into multiple diffraction orders.

A 100X oil-immersion objective with NA=1.4 (Nikon PLAN APO), is used to focus these diffraction orders on the microscope cover slip sample (glass, #0, thickness ~0.1 mm, coated with 50 nm thick uniform layer of Au).

Due to the tight focusing scheme, phase-matching condition for the SPP mode propagating on the Au-air interface is achieved and thus the illuminating beam of light is coupled to this SPP mode. The near-field of the SPPs is collected by an NSOM, (Nanonics Imaging Ltd. Multiview 4000), using Cr-Au coated NSOM probes, with typical aperture diameters of 250-300 nm. The collected signal is detected and amplified by an IR femto-Watt InGaAs photoreceiver (New-focus Inc. model 2153) connected to a lock-in amplifier (Stanford Research Systems Inc. SR830). To operate the lock-in scheme the laser beam is externally modulated at 580 Hz.

Dammann gratings are well known for their capability of splitting an optical beam into multiple diffraction orders with equal intensity. We have designed the gratings to produce 9 equal-intensity diffraction orders in a 3X3 array. We designed two grating structures with period lengths of $\Lambda_1 = 100 \mu\text{m}$, and $\Lambda_2 = 400 \mu\text{m}$. Ultimately only the latter was used, due to the shorter lateral distances between diffraction orders. Optimal phase-transition point was calculated to be $ax_1 = 0.735\Lambda$, and the grating height was designed to provide π phase delay.

The gratings were fabricated by photolithography followed by reactive ion etching to transfer the pattern into glass. First, a 100 nm thick layer of Chromium was deposited on the glass substrate. Next, a photo resist was spun on top of the metal layer and exposed to a photomask. The pattern was transferred to the metal layer which in turn was used as a mask for the reactive ion etching of the glass. Grating depth in the glass was ~1.2 μm which translates to the desired phase-shift of nearly π .

The gratings were characterized by placing them in the back focal plane of a lens with focal length $f = 10 \text{ cm}$, and placing a CCD camera in the front focal plane. Illuminating from behind the grating generates the exact Fourier transform of the grating on the CCD (see Fig. 12). Fig. 12a shows the array of donut shaped radially polarized diffraction orders. Fig. 12b shows the same image, now with a linear polarizer placed in front of the CCD.

As can be seen, two lobes appear along the axis for which the direction of the radial polarization coincides with the polarizer axis. Rotating the analyzer by 90 degrees results in similar rotation of the two lobes. Measuring the intensity of each diffraction order we found that the central (0th) order is 15% brighter than other orders, due to imperfections in the fabrication.

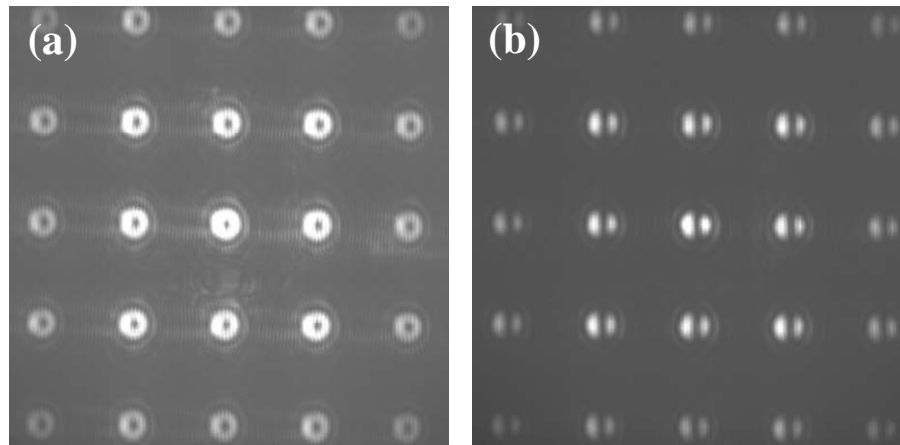


Fig. 12. (a) Far-field diffraction images of a radially polarized beam after passing through the Dammann grating. (b) Same as (a) but with a linear polarizer (aligned to block the vertical polarization component) placed in-front of the CCD.

After verifying the operation of the Dammann grating, we turned into the near field measurements of the SPPs on the metal film. First, we illuminated the sample with a single radially polarized beam. The results are presented in Fig. 13. Fig. 13a shows the NSOM scan over an area of 10 by 10 microns. Fig. 13b shows a cross section along the white dashed line of Fig. 4a. The experimental result agrees quantitatively (in period) and qualitatively (in intensity) with the theoretical fit.

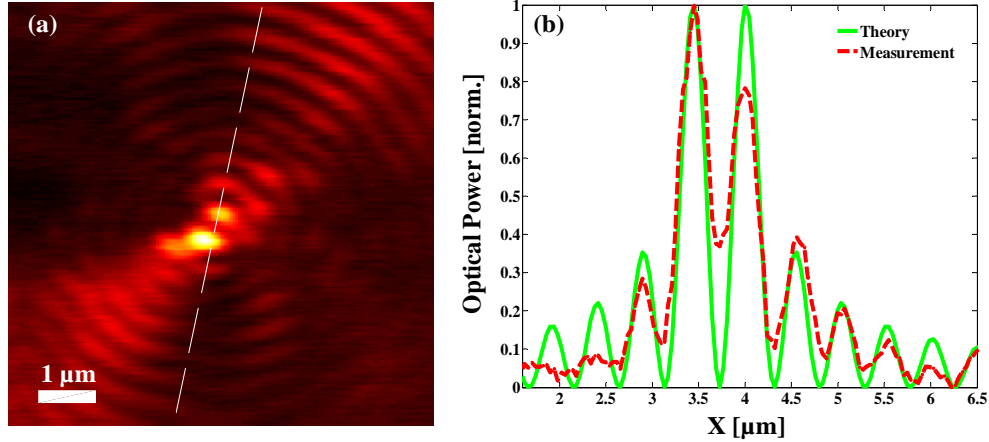


Fig. 13. (a) an NSOM scan of a single plasmonic focal spot. (b) Dashed red line - a cross section of the measured result presented in Fig. 13a along the white dashed line. Solid green line – the theoretical intensity pattern.

Next, we repeated the measurement, this time with the Dammann grating presented in the optical path to obtain the 3X3 spot array. The NSOM measurement results are displayed in linear scale (Fig. 14a) and in logarithmic scale (Fig 14b). One can clearly observe the interference patterns between the different diffraction orders, which are the result of the coherent interactions between the multiple radially polarized plasmonic sources. While coherent interactions on flat metallic surfaces were demonstrated before, e.g. using excitation from multiple nanoslits, this is the first time that the multiple plasmonic sources are generated by the structured illumination function rather than by patterning the sample.

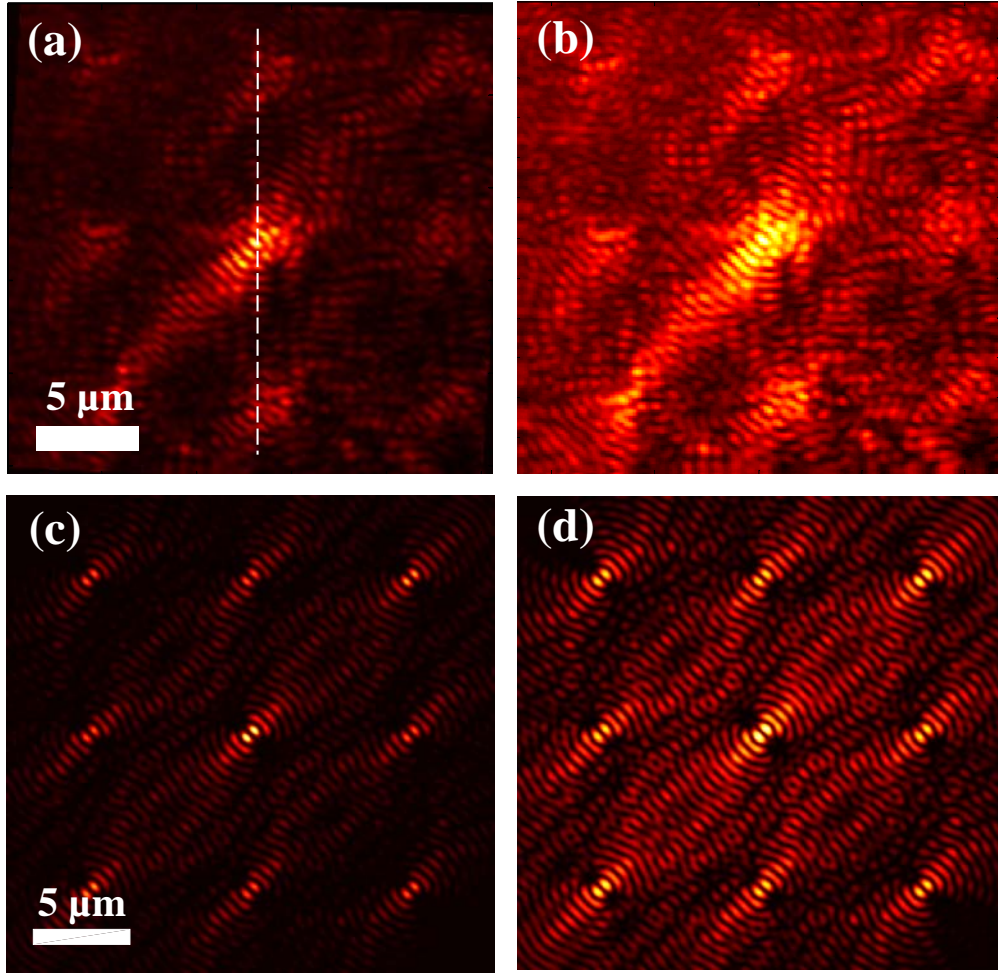


Fig. 14 (a) NSOM scan of the metal film illuminated by a 3X3 spot array in normal intensity scale. The dashed line provides a mark for the cross section presented in the next Figure. (b) Same as (a) but in logarithmic scale for better visibility of the interference fringes. (c) Simulation results showing the calculated intensity of the transverse electric field component. A polarizer was apply to transmit only the polarization direction aligned with the diagonal from lower left to the upper right of the Figure, taking into account the polarization properties of our bended NSOM probe. (d) Same as (c) but in logarithmic scale for better visibility of the interference fringes.

By comparing the experimental results to the computer simulation, common features can be clearly identified. However, the experimental results show strong response for light polarized along the diagonal axis running from the lower left to the upper right corner of the figure. We attribute this observation to the effect of polarization response in our NSOM probes. These probes are bended, with their bending axis perpendicular to the above mentioned diagonal. As a result, the signal polarized along the bending axis is suppressed upon propagation in the bended probe. To account for this effect we re-sketch simulated distribution, this time after taking into account the effect of polarization selective collection efficiency. The results are shown in Fig. 14c (in linear scale) and Fig. 14d (in logarithmic scale). The nice agreement between experiment and theory can now be clearly observed.

To further stress the agreement between experiment and theory, we plot a cross section of the experimental result along the white dashed line shown in Fig. 14a, together with the theoretical cross section taken from Fig. 14c. The results are presented in Fig. 15. Comparing the two curves, one can see that both the interference fringes and the general trend of the envelope function are in good agreement.

Another interesting observation is that the central hot spot appears to be almost three times stronger with respect to the other spots. The difference cannot be explained by the deviations in our Dammann grating (15%). Clearly, the coherent interactions between the different diffraction orders via SPP modes generate differences between the intensities of the focal spots. However, if we allocate similar amplitude to all diffraction orders we still do not observe such a drastic intensity difference in the simulation. In order to

observe this difference in intensity we allocated a $\sqrt{2}$ larger amplitude value to the central diffraction order, as previously mentioned in the simulation section. We believe that the need to allocate different values of amplitude to different plasmonic spots may be the result of a difference in coupling efficiency of the various diffraction orders to SPPs.

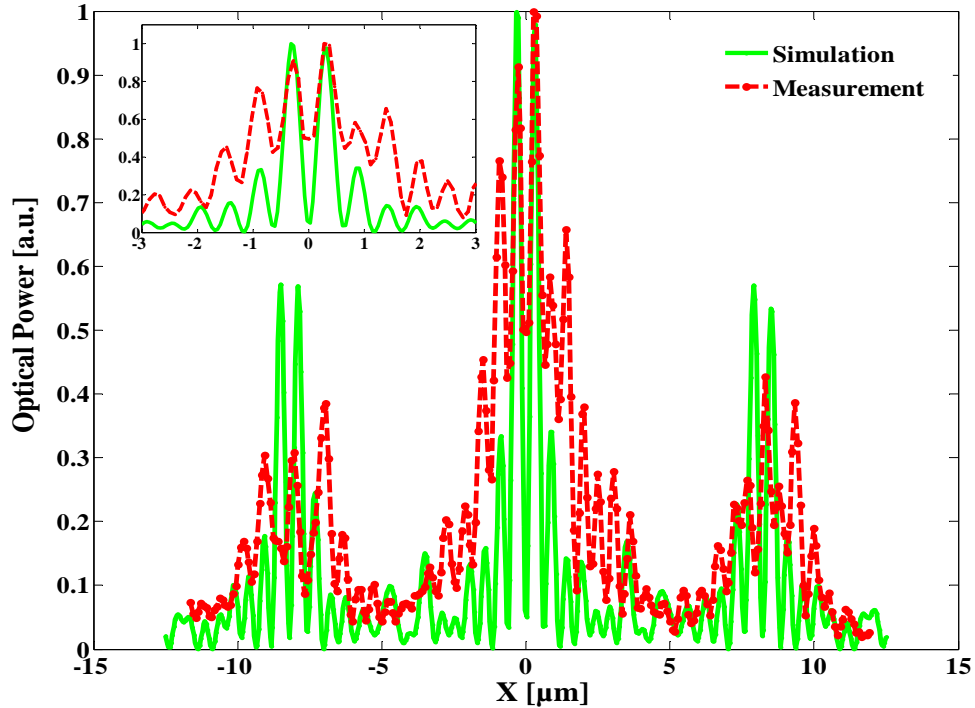


Fig. 15. Cross-sections of the experimental results (dashed red line) and the simulation results (solid green line) along the white dashed line marked in Fig. 14a. Inset – Zoom in on the central region.

To summarize, we have demonstrated the coupling of an array of radially polarized spots to surface plasmon polaritons (SPPs) propagating on a uniform Au film. This was achieved by splitting a radially polarized beam using a phase Dammann grating into 3X3 array of diffraction orders which are tightly focused onto the metal film with the aid of a high N.A oil immersion microscope objective.

The demonstrated setup overcomes one of the major deficiencies of radially polarized light, i.e. the existence of a single origin, thus allowing taking advantage of the previously demonstrated advantages of radially polarized light in coupling to SPPs and in generating sharper plasmonic hot spots and expand its applicability in applications involving parallel processing.

The SPP field propagating on the metal-air interface was measured by NSOM. We observed strong interference patterns which are the result of coherent interactions between the plasmonic sources propagating towards each other. It should be noted that unlike the typical case where the plasmonic patterns are originated from the structure of the sample (e.g. nanoholes or nanoslits), here the coherent interactions are the result of the structured illumination pattern.

The experimental results are in good agreement with the theory, showing interference fringes having periodicity compatible with the plasmonic SPP wavelength. The measured envelope of the diffraction pattern agrees qualitatively with the simulation results. The measurements show preferred response for light polarized in the direction oriented at 45 degrees with respect to the horizontal axis of the figure. This finding is explained by the polarization response properties of our bended NSOM probe. Finally, the demonstrated approach of generating array of radially polarized plasmonic hot spots on flat metallic film, may be used in myriad applications e.g. microscopy, lithography, sensing and optical memories.

Journal publications and conference presentations:

1 - G. Lerman and U. Levy, "Pin Cushion Plasmonic Device for Polarization Beam Splitting, Focusing, and Beam Position Estimation", Nano Lett. 13, 1100-1105 (2013).

- 2 - G. Lerman and U. Levy, "Polarization Based Plasmonic Splitter and Focusing Device," CLEO ,San Jose, 2012. Paper QM2K.2.
- 3 - J. Bar-David, G. M. Lerman, L. Stern, N. Mazurski, and U. Levy, "Generation of a periodic array of radially polarized Plasmonic focal spots," Opt. Express 21, 3746-3755 (2013).
- 4 - J. Bar-David, N Mazurski, G. M. Lerman, L. Stern, and Uriel Levy, "Coherent interactions between multiple radially polarized plasmonic sources," Nano Meta, Seefeld (2013), Paper SAT5f.28.
- 5 - J. Bar-David, N Mazurski, G. M. Lerman, L. Stern, and Uriel Levy, Generation of a periodic array of radially polarized Plasmonic focal spots SPP6, Ottawa (2013). Paper Tu-28-P-66